

This is the accepted manuscript made available via CHORUS. The article has been published as:

Polarized proton+^{4,6,8}He elastic scattering with breakup effects in the eikonal approximation

K. Kaki, Y. Suzuki, and R. B. Wiringa

Phys. Rev. C **86**, 044601 — Published 1 October 2012

DOI: [10.1103/PhysRevC.86.044601](https://doi.org/10.1103/PhysRevC.86.044601)

Polarized proton+^{4,6,8}He elastic scattering with breakup effects in the eikonal approximation

K. Kaki*

Department of Physics, Shizuoka University, Shizuoka 422-8529, Japan

Y. Suzuki

*Department of Physics, Niigata University, Niigata 950-2181, Japan and
RIKEN Nishina Center, Wakko 351-0198, Japan*

R. B. Wiringa

*Physics Division, Argonne National Laboratory, Argonne, Illinois 60439, USA
(Dated: August 27, 2012)*

We study the elastic scattering of polarized protons from He isotopes. The central and spin-orbit parts of the optical potential are derived using the Glauber theory that can naturally take account of the breakup effect of the He isotopes. Both the differential cross section and the vector analyzing power for $p+^{4,6,8}\text{He}$ scattering at 71 MeV are in reasonable agreement with experiment. Scattering observables at 300 MeV are predicted. The Pauli blocking effect is examined at 71 MeV.

PACS numbers: 25.40.Cm, 24.70.+s, 24.10.Ht, 21.10.Gv, 21.60.De

Keywords: Glauber model, vector analyzing power, He isotopes, breakup effect

I. INTRODUCTION

The spin-orbit potential for a nucleon moving in a nucleus plays a decisive role in the nuclear shell structure. Though the phenomenological aspect of the spin-orbit potential has been clarified rather well for stable nuclei, a full account of its origin is still under active study. Important information on the spin-orbit potential is obtained through the analysis of elastic scattering observables, especially a vector analyzing power in the elastic scattering of polarized protons from the nucleus.

Recent developments of experimental techniques have provided us with a polarized proton target and have made it possible to measure not only the differential cross section but also the vector analyzing power for the elastic scattering of polarized protons from unstable nuclei in the inverse kinematics. The data have recently been taken for ^6He [1] and ^8He [2] at 71 MeV/nucleon. A good example of a two-neutron halo nucleus is ^6He , where the neutron density extends far out in distance. This unique feature of its structure is expected to show up in the vector analyzing power because the spin-orbit potential is primarily sensitive to the surface of the nucleus. Though less pronounced than ^6He , ^8He has an extended neutron cloud as well and its elastic scattering observables are interesting.

There have been so far a few theoretical studies on the optical potential and observables for $p+^{6,8}\text{He}$ elastic scattering. The single scattering approximation to the multiple scattering expansion was employed in the $p+^8\text{He}$ case [3]. The predicted angular distribution of the vector analyzing power shows a peak at about $\theta_{\text{c.m.}}=46^\circ$, dif-

ferent from the data [2]. The $p+^8\text{He}$ elastic scattering angular distribution was analyzed in the eikonal model to examine the sensitivity to the matter distribution of ^8He [4]. The $p+^{6,8}\text{He}$ elastic scattering observables were calculated in a full-folding optical model [5]. The calculated vector analyzing powers do not agree with experiment [1, 2]. Very recently the neutron pickup coupling with the elastic channel has been studied to see its effect on proton scattering from ^6He [6]. As noted above, none of the calculations succeeds in reproducing the vector analyzing powers for $p+^{6,8}\text{He}$ scattering. It is reported that a search for the optical potential parameters of the spin-orbit part leads to a shallow and long-ranged spin-orbit potential for ^6He [1].

The purpose of this paper is to analyze the elastic scattering observables, the differential cross section, the vector analyzing power and the spin-rotation function, for protons scattered from the He isotopes including ^4He [7]. The central part of the optical potential for the proton is calculated in the framework of Glauber or the eikonal model [8]. The inputs needed in the calculation include only the ground state wave functions of the He isotopes and the nucleon-nucleon scattering amplitude, or more precisely its Fourier transform, the nucleon-nucleon profile function. The spin-orbit potential is constructed using a derivative of the central part of the optical potential. There are at least three noticeable advantages of the present approach: Firstly it is logically very simple, and nevertheless contains nucleon-nucleon multiple scatterings to all orders. Secondly the wave function of the projectile nucleus itself can be employed, though in an approximate version of the present approach the projectile density may be used instead of the wave function. Thirdly the optical potential obtained takes account of breakup effects of the projectile without recourse to laborious calculations with continuum discretization [9, 10],

* spkkaki@ipc.shizuoka.ac.jp

which enables us to discuss easily a dynamic polarization potential (DPP). The breakup effect is a vital ingredient that should be taken care of for the optical potential of a weakly bound nucleus like ${}^6\text{He}$.

In Sec. II we present a formulation needed in our approach. We show in Sec. II A how to construct the optical potential, its approximate version and a relationship between those potentials and a folding potential. We define our spin-orbit potential in Sec. II B together with the elastic scattering observables. In Sec. II C we outline the variational Monte Carlo method that is employed to generate the ground state wave functions of the He isotopes. Results of calculation are presented in Sec. III. First we compare the elastic scattering observables at 71 MeV/nucleon with experiment in Sec. III A. The angular distributions of the differential cross section and vector analyzing power for $p+{}^4\text{He}$ scattering at higher energies are compared to available data in Sec. III B. Predictions for $p+{}^{6,8}\text{He}$ scattering at intermediate energy are also given. Conclusions are drawn in Sec. IV.

II. FORMULATION

A. Optical potential in the eikonal approximation

Let us assume that the projectile nucleus moves in the z direction and impinges on a proton target with a velocity v . Let \mathbf{R} stand for the relative distance vector between the projectile and the proton. Under the eikonal approximation the x, y component of \mathbf{R} , denoted \mathbf{b} , turns out to be just a parameter, the impact parameter. The interaction v_{pN} between the i th nucleon of the projectile and the proton gives rise to a multiplicative phase factor $e^{i\chi_{pN}(\mathbf{b}-\mathbf{s}_i)}$ [8] that modifies the wave function of the projectile, where \mathbf{s}_i is the x, y component of the position vector \mathbf{r}_i of the i th nucleon relative to the center of mass of the projectile. The phase χ_{pN} is related to v_{pN} by

$$\chi_{pN}(\mathbf{b}) = -\frac{1}{\hbar v} \int_{-\infty}^{+\infty} v_{pN}(\sqrt{\mathbf{b}^2 + z^2}) dz. \quad (1)$$

Each nucleon contributes the position-dependent multiplicative phase factor. A key quantity to describe the proton-projectile elastic scattering is given by the eikonal phase

$$e^{i\chi_E(\mathbf{b})} = \langle \Phi_0 | e^{i\Xi(\mathbf{b}, \mathbf{s}_1, \dots, \mathbf{s}_A)} | \Phi_0 \rangle, \quad (2)$$

where $\Xi(\mathbf{b}, \mathbf{s}_1, \dots, \mathbf{s}_A) = \sum_{i=1}^A \chi_{pN}(\mathbf{b} - \mathbf{s}_i)$ is the total phase, and Φ_0 is the ground state wave function of the projectile nucleus.

As is well-known [9, 10], the optical phase shift function (2) obtained in the eikonal approximation includes the effects of coupling with excited states or breakup continuum states. To make this point clear, we define the average of the total phase

$$\chi_F(\mathbf{b}) = \langle \Phi_0 | \Xi(\mathbf{b}, \mathbf{s}_1, \dots, \mathbf{s}_A) | \Phi_0 \rangle. \quad (3)$$

Hereafter the projectile nucleus is assumed to be spherical, so that both $\chi_E(\mathbf{b})$ and $\chi_F(\mathbf{b})$ become a function of $b = |\mathbf{b}|$. Using Eqs. (1) and (3), we find that $\chi_F(b)$ is the phase shift function corresponding to the single folding potential $U_f(R) = \int \rho_N(r) v_{pN}(|\mathbf{R} - \mathbf{r}|) d\mathbf{r}$

$$\chi_F(b) = -\frac{1}{\hbar v} \int_{-\infty}^{+\infty} U_f(\sqrt{\mathbf{b}^2 + z^2}) dz, \quad (4)$$

where $\rho_N(r)$ is the nucleon density of the projectile nucleus. The eikonal phase $\chi_E(b)$ is expressed as follows

$$\chi_E(b) = \chi_F(b) - i \ln \langle \Phi_0 | e^{i(\Xi(\mathbf{b}, \mathbf{s}_1, \dots, \mathbf{s}_A) - \chi_F(b))} | \Phi_0 \rangle. \quad (5)$$

According to Glauber [8], a potential $U_c(R)$

$$U_c(R) = \frac{\hbar v}{\pi} \frac{1}{R} \frac{d}{dR} \int_0^\infty \chi_E(\sqrt{R^2 + x^2}) dx \quad (6)$$

produces the phase shift function $\chi_E(b)$ in the eikonal approximation. The potential $U_c(R)$ differs from $U_f(R)$ in that the underlying phase shift function of the former contains the second term of the right-hand side of Eq. (5). The term can be discussed in a cumulant expansion [8, 10] that involves the fluctuation of the higher order cumulants $\langle \Phi_0 | (\Xi(\mathbf{b}, \mathbf{s}_1, \dots, \mathbf{s}_A) - \chi_F(b))^n | \Phi_0 \rangle$. The difference between $U_c(R)$ and the folding potential $U_f(R)$ is the DPP. As is clear from the above derivation, the DPP is evaluated in the eikonal approximation without an explicit invoking of the couplings with excited and continuum states.

It should be stressed that the central part of the optical potential $U_c(R)$ can be obtained in a unified way independently of the projectile nucleus.

The above formulation has successfully been applied to a study of the breakup effects of weakly bound projectile nuclei, e.g., d scattered from ${}^{58}\text{Ni}$ [9] and ${}^6\text{He}$ scattered from ${}^{12}\text{C}$ [11]. In these applications the target is not a proton but a composite nucleus. It is treated as an absorbing point particle and then it is possible to apply exactly the same formulation as above by adopting appropriate nucleon-target optical potentials for v_{pN} . The quality of such calculations is tested by comparing to other calculations that explicitly include the breakup channels in continuum discretized coupled-channels method [12, 13].

For the proton target, v_{pN} stands for the proton-nucleon potential. Any operator dependence of the potential has to be avoided because otherwise the evaluation of Eq. (2) together with Eq. (1) is impossible. Instead of looking for some effective forces that have no operator dependence, we follow a simple procedure here. We introduce the proton-nucleon profile function $\Gamma_{pN}(\mathbf{b})$, which is equal to $1 - e^{i\chi_{pN}(\mathbf{b})}$. With $\Gamma_{pN}(\mathbf{b})$, the proton-nucleon scattering amplitude $f_{pN}(\theta)$ is given in the eikonal approximation by

$$f_{pN}(\theta) = \frac{iK}{2\pi} \int e^{-i\mathbf{q} \cdot \mathbf{b}} \Gamma_{pN}(\mathbf{b}) d\mathbf{b}, \quad (7)$$

where K is the wave number and \mathbf{q} is the momentum transfer, $q=2K \sin \frac{\theta}{2}$, and $\Gamma_{pN}(\mathbf{b})$ is conveniently parametrized as

$$\Gamma_{pN}(\mathbf{b}) = \frac{1 - i\alpha_{pN}}{4\pi\beta_{pN}} \sigma_{pN}^{\text{tot}} e^{-\frac{b^2}{2\beta_{pN}}}, \quad (8)$$

where α_{pN} is the ratio of the real to the imaginary part of the pN scattering amplitude in the forward direction, β_{pN} is the slope parameter of the pN elastic differential cross section, and σ_{pN}^{tot} is the pN total cross section due to the nuclear pN interaction. We use the parameter values tabulated in Ref. [14]. The difference between pp and pn interactions is taken into account in what follows by extending Eq. (8) to

$$\Gamma_{pN}(\mathbf{b}) = \delta_{Np}\Gamma_{pp}(\mathbf{b}) + \delta_{Nn}\Gamma_{pn}(\mathbf{b}). \quad (9)$$

In this way we bypass the direct use of the nuclear force in calculating $\chi_E(b)$.

The eikonal phase $\chi_E(b)$ and the average total phase $\chi_F(b)$ are expressed in terms of the profile function as follows

$$\chi_E(b) = -i \log \langle \Phi_0 | \prod_{i=1}^A (1 - \Gamma_{pN}(\mathbf{b} - \mathbf{s}_i)) | \Phi_0 \rangle, \quad (10)$$

$$\chi_F(b) = -i \int \rho_N(r) \log (1 - \Gamma_{pN}(\mathbf{b} - \mathbf{s})) d\mathbf{r}. \quad (11)$$

Both neutron and proton densities are employed in calculating $\chi_F(b)$. As will be explained in Sec. II C, $\chi_E(b)$ is obtained with a Monte Carlo integration. It turns out that the present approach together with the Monte Carlo integration is very versatile for calculating the eikonal phase and the corresponding optical potential. A simpler calculation is to take the leading order of the cumulant expansion, leading to

$$\chi_E^{(1)}(b) = i \int \rho_N(r) \Gamma_{pN}(\mathbf{b} - \mathbf{s}) d\mathbf{r}. \quad (12)$$

This provides us with a reasonable approximation to the full phase for the nucleon-nucleus scattering, and is often adopted for the evaluation of the phase shift function

for the scattering between complex nuclei [14–16]. Equation (6) is used to obtain those potentials which generate the phases $\chi_F(b)$ and $\chi_E^{(1)}(b)$, and they are compared with $U_c(R)$.

B. Elastic scattering observables

The potential $U_c(R)$ constructed in this way is central and includes the effect of breakup of the projectile in the eikonal approximation. The spin-orbit term of the optical potential is introduced as

$$U_{\text{so}}(R) = V_{\text{so}} \lambda_\pi^2 \frac{1}{R} \frac{d}{dR} U_c(R), \quad (13)$$

where λ_π is the pion Compton wavelength. The real and imaginary parts of the spin-orbit potential are thus obtained from the real and imaginary parts of U_c , respectively and the constant V_{so} that determines the spin-orbit strength is allowed to be different depending on the real and imaginary parts of the spin-orbit potential.

Proton-nucleus scattering is described in a partial wave expansion with the potential $U_c(R) + \mathbf{l} \cdot \boldsymbol{\sigma} U_{\text{so}}(R)$. The scattering amplitude becomes an operator in the spin space

$$\hat{f}(\theta) = f(\theta) + ig(\theta) \boldsymbol{\sigma} \cdot \hat{\mathbf{n}} \quad (14)$$

with a unit vector $\hat{\mathbf{n}}$ perpendicular to the scattering plane

$$\hat{\mathbf{n}} = \frac{\mathbf{k} \times \mathbf{k}'}{|\mathbf{k} \times \mathbf{k}'|}, \quad (15)$$

where \mathbf{k} and \mathbf{k}' are the momenta in the center of mass before and after the scattering. Denoting the S matrix by $S_l^\pm = \exp(2i\delta_l^\pm)$ where δ_l^\pm are complex phase shifts for the potential $U_c(R) + lU_{\text{so}}(R)$ or $U_c(R) - (l+1)U_{\text{so}}(R)$, respectively, we obtain

$$f(\theta) = f_C(\theta) + \frac{1}{2ik} \sum_l [(l+1)(S_l^+ - 1) + l(S_l^- - 1)] e^{2i\delta_l^C} P_l(\cos \theta), \quad (16)$$

$$g(\theta) = \frac{1}{2ik} \sum_l (S_l^+ - S_l^-) e^{2i\delta_l^C} P_l^1(\cos \theta), \quad (17)$$

where $f_C(\theta)$ is the Coulomb scattering amplitude, δ_l^C is the Coulomb phase shift, and $P_l^1(\theta)$ is the associated Legendre polynomial. A deviation of the Coulomb potential from that of a point charge is included in the calculation but its effect is very small.

For a fixed angle θ the scattering amplitude \hat{f} is determined by three real quantities. They can be conventionally chosen as the differential cross section $d\sigma/d\Omega$, the vector analyzing power A_y , and the spin-rotation func-

tion Q :

$$\frac{d\sigma}{d\Omega} = |f(\theta)|^2 + |g(\theta)|^2, \quad (18)$$

$$A_y(\theta) = \frac{2\text{Re}(f(\theta)g^*(\theta))}{|f(\theta)|^2 + |g(\theta)|^2}, \quad (19)$$

$$Q(\theta) = \frac{2\text{Im}(f(\theta)g^*(\theta))}{|f(\theta)|^2 + |g(\theta)|^2}. \quad (20)$$

C. Variational Monte Carlo wave function

The wave functions of He isotopes used in this work are taken from variational Monte Carlo (VMC) calculations for a Hamiltonian consisting of nonrelativistic nucleon kinetic energy, the Argonne v_{18} two-nucleon potential [17], and the Urbana IX three-nucleon potential [18]:

$$H = \sum_i K_i + \sum_{i<j} v_{ij} + \sum_{i<j<k} V_{ijk}. \quad (21)$$

A VMC calculation finds an upper bound E_V to an eigenenergy E_0 of the Hamiltonian by evaluating the expectation value of H in a trial wave function, Ψ_V :

$$E_V = \frac{\langle \Psi_V | H | \Psi_V \rangle}{\langle \Psi_V | \Psi_V \rangle} \geq E_0. \quad (22)$$

Parameters in Ψ_V are varied to minimize E_V , and the lowest value is taken as the approximate energy. The multidimensional integral is evaluated using standard Metropolis Monte Carlo techniques [19], hence the VMC designation. A good trial function is given by [20]

$$|\Psi_V\rangle = \mathcal{S} \prod_{i<j}^A \left[1 + U_{ij} + \sum_{k \neq i,j}^A \tilde{U}_{ijk} \right] |\Psi_J\rangle, \quad (23)$$

where U_{ij} and \tilde{U}_{ijk} are non-commuting two- and three-body correlation operators induced by the dominant parts of v_{ij} and V_{ijk} , respectively; \mathcal{S} is a symmetrizer, and the Jastrow wave function Ψ_J is

$$|\Psi_J\rangle = \prod_{i<j} f_c(r_{ij}) |\Phi_A(J^\pi; TT_z)\rangle. \quad (24)$$

Here the single-particle A -body wave function $\Phi_A(J^\pi; TT_z)$ is fully antisymmetric and has the total spin, parity, and isospin quantum numbers of the state of interest, while the product over all pairs of the central two-body correlation $f_c(r_{ij})$ keeps nucleons apart to avoid the strong short-range repulsion of the interaction. The long-range behavior of f_c and any single-particle radial dependence in Φ_A (which, to ensure translational invariance, is written using coordinates relative to the center of mass of the s-shell core) control the finite extent of the nucleus. For p-shell nuclei, there are actually three different central pair correlation functions f_c : f_{ss} , f_{sp} , and f_{pp} , depending on whether both particles are in the s-shell core (ss), both in the p-shell valence regime (pp), or one in each (sp).

The two-body correlation operator has the structure

$$U_{ij} = \sum_{p=2,6} u_p(r_{ij}) O_{ij}^p, \quad (25)$$

where the O_{ij}^p are the leading spin, isospin, spin-isospin, tensor, and tensor-isospin operators in v_{ij} . The radial shapes of $f_c(r)$ and $u_p(r)$ are obtained by numerically solving a set of six Schrödinger-like equations: two single-channel for $S=0$, $T=0$ or 1, and two coupled-channel for $S=1$, $T=0$ or 1, with the latter producing the important tensor correlations [21]. These equations contain the bare v_{ij} and parametrized Lagrange multipliers to impose long-range boundary conditions of exponential decay and tensor/central ratios.

Perturbation theory is used to motivate the three-body correlation operator

$$\tilde{U}_{ijk} = -\epsilon \tilde{V}_{ijk}(\tilde{r}_{ij}, \tilde{r}_{jk}, \tilde{r}_{ki}) \quad (26)$$

where $\tilde{r} = yr$, y is a scaling parameter, ϵ is a (small negative) strength parameter, and \tilde{V}_{ijk} includes the dominant short-range repulsion and anticommutator part of two-pion exchange in the three-nucleon potential. Consequently, \tilde{U}_{ijk} has the same spin, isospin, and tensor dependence that \tilde{V}_{ijk} contains.

The variational parameters in f_{ss} , U_{ij} , and \tilde{U}_{ijk} have been chosen to minimize the energy of the s-shell nucleus ^4He . For the p-shell nuclei ^6He and ^8He , these parameters are kept fixed and the additional parameters that enter f_{sp} , f_{pp} , and the single-particle radial behavior of Φ_A have been adjusted to minimize the energy of these systems subject to the constraint that the proton and neutron rms radii are close to those obtained from more sophisticated Green's function Monte Carlo (GFMC) calculations [20, 22].

The wave function samples used here are generated by following a random walk guided by the Ψ_V for each nucleus. After an initial randomization, a move is attempted, where each particle is randomly shifted within a box of 1.2-1.4 fm in size; the Ψ_V is evaluated and compared to the previous configuration, with the move being accepted or rejected according to the Metropolis algorithm. After ten attempted moves, the configuration is saved, including the x, y, z coordinates of each particle (the center of mass is set to zero) and the probability for each particle to be either a neutron or a proton. The size of the box gives an acceptance rate of $\sim 50\%$ and we generate one million configurations for each nucleus.

The root-mean-square radii calculated from the VMC wave functions are listed in Table I. The second column shows the proton root-mean-square radii extracted from the charge radii that are obtained from the experiment based on laser spectroscopy [23]. The results of the VMC wave functions excellently reproduce the radii determined experimentally.

The density distributions of He isotopes are displayed in Fig. 1. Solid and dotted lines denote the neutron and proton distributions, respectively. Both proton and neutron distributions of ^4He are almost the same and are

TABLE I. Root-mean-square radii, given in units of fm, of the proton and neutron distributions of ${}^4, {}^6, {}^8\text{He}$. The proton radius of the second column is obtained by converting the measured charge radius.

| He isotope | Expt. [23] proton | Calc. | |
|-----------------|----------------------|--------|---------|
| | | proton | neutron |
| ${}^4\text{He}$ | 1.457(4) | 1.447 | 1.447 |
| ${}^6\text{He}$ | 1.938(23) | 1.928 | 2.871 |
| ${}^8\text{He}$ | 1.885(48) | 1.884 | 2.901 |

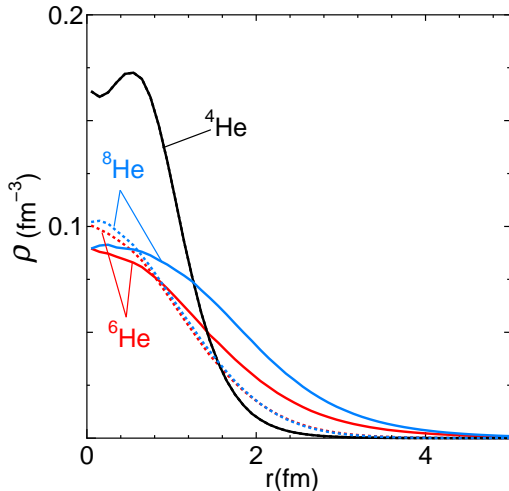


FIG. 1. (Color online) Density distributions of ${}^4, {}^6, {}^8\text{He}$ calculated with the VMC wave functions. Solid and dotted lines denote the neutron and proton distributions, respectively.

confined to the small region. Though the proton distribution is very similar in both ${}^6\text{He}$ and ${}^8\text{He}$, the tail of ${}^6\text{He}$ is slightly more extended to larger distances. Beyond 2 fm, the neutron distribution overwhelms that of proton. The falloff of ${}^6\text{He}$ neutron density is rather slow compared to that of ${}^8\text{He}$ owing to its weak binding.

III. RESULTS

The construction of the optical potential, (6) and (13), requires the 3A-dimensional integration indicated in Eq. (2) or (10). This integration can be performed with ease in the Monte Carlo method using the wave function samples generated in Sec. II C. The feasibility and the accuracy of the Monte Carlo integration in the calculation of the phase shift function was already demonstrated for various cases in Ref. [24]. The differentiation in Eq. (6) is facilitated by fitting $\chi_E(b)$ in terms of several Gaussians with different falloff parameters: $\chi_E(b) = \sum_k C_k \exp(-a_k b^2)$.

TABLE II. Strength parameters V_{so} of the spin-orbit potentials for $p+{}^4, {}^6, {}^8\text{He}$ scattering at 71 MeV.

| He isotope | Real potential | Imaginary potential |
|-----------------|----------------|---------------------|
| ${}^4\text{He}$ | 0.125 | -0.075 |
| ${}^6\text{He}$ | 0.025 | 0.00 |
| ${}^8\text{He}$ | 0.05 | 0.00 |

A. Scattering at 71 MeV

First we discuss the elastic scattering observables at 71 MeV. The strength V_{so} of the spin-orbit potential is the only parameter in the present formalism. The differential cross section is largely determined by the central potential U_c . The spin-orbit potential contributes to the differential cross section almost negligibly within a reasonable range of the strength, and so we try to fit the vector analyzing power by varying V_{so} . In the case of ${}^4\text{He}$, we choose different values of the strength parameter depending on the spin-orbit real or imaginary potential. The spin-orbit imaginary potential for ${}^6\text{He}$ and ${}^8\text{He}$ is set to be zero for the sake of simplicity. The depth parameters of the spin-orbit potential are listed in Table II. The value of V_{so} for the $p+{}^4\text{He}$ spin-orbit real potential is consistent with that employed in the systematics of one-particle motion [25]. Compared to ${}^4\text{He}$, the strength of the spin-orbit real potential for ${}^6, {}^8\text{He}$ is considerably smaller, in accordance with the analysis of Ref. [1].

Figure 2 shows the optical potentials calculated for $p+{}^4, {}^6, {}^8\text{He}$ elastic scattering. The left and right panels of Fig. 2(a) are the central real and imaginary potentials. Solid lines denote potentials of the full calculation, while dash-dotted lines are the folding potentials. The optical potential for ${}^4\text{He}$ is much deeper than the others at short distances due to its compact structure but becomes much shallower near the surface. Compared to the folding potential, the full optical potential has the following property near the surface: the imaginary part turns out to be much more absorptive and the real part is less attractive. This is a general feature of the DPP due to the breakup effect as already observed in Ref. [9]. Similarly Fig. 2(b) exhibits the spin-orbit real and imaginary potentials.

Figure 3 displays the differential cross sections (upper panels) and vector analyzing powers (lower panels) for ${}^4\text{He}$, ${}^6\text{He}$ and ${}^8\text{He}$ calculated using the above potentials. Solid lines denote the results based on the potential derived from the full phase shift function (10), dotted lines are the results obtained from its leading order in the cumulant expansion (12), and dash-dotted lines are the results of the folding potential (11). It is seen that the full potential gives smaller and better differential cross sections than the folding potential. The vector analyzing powers are also better reproduced with the full potential. The leading order approximation seems to be surprisingly good. The vector analyzing power available for ${}^4\text{He}$ is accurately known [7], and its behavior that changes a sign

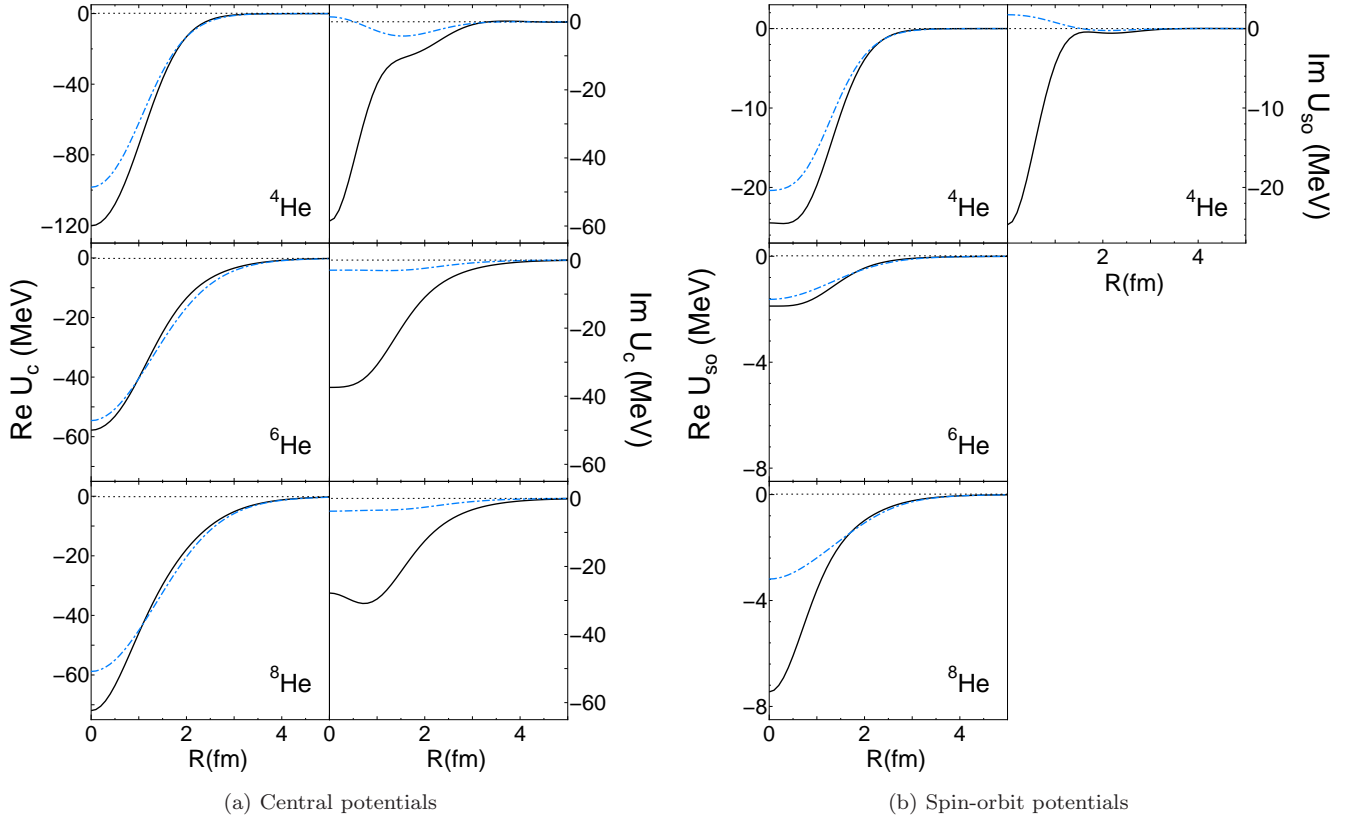


FIG. 2. (Color online) Optical potentials for $p+^{4,6,8}\text{He}$ elastic scattering at 71 MeV. The central and spin-orbit potentials are shown in Fig. 2(a) and 2(b), respectively. The left and right panels are the real and imaginary potentials, respectively. The spin-orbit imaginary potentials of ^6He and ^8He are set to be zero. Solid and dash-dotted lines are the potentials of the full eikonal model and the folding model, respectively.

around 60 degrees demands a nonvanishing V_{so} value for the imaginary potential. In Ref. [6] the effects of a DPP due to pickup coupling has been studied on the differential cross section and vector analyzing power for proton elastic scattering from ^6He . Their results for full calculation including both pickup and breakup contributions have shown a decrease in the differential cross section around 50 degrees and an increase in the vector analyzing power in angles larger than 50 degrees, which is in disagreement with the data.

Though the present theory reproduces the experimental data – especially the vector analyzing powers – fairly well, the calculated differential cross sections tend to be large compared to experiment. The incident energy of 71 MeV is likely not to be high enough for the Glauber approximation. In such a case that the incident energy of the projectile is comparable to its Fermi energy, the use of the information on the free space nucleon-nucleon interaction may not be valid, but Pauli-blocking effects may become important. In fact the chance for the incident nucleon to collide with the proton target will be suppressed because of the Pauli effect.

To simulate this Pauli-blocking correction phenomeno-

logically, we replace the σ_{pN}^{tot} value of Eq. (8) with

$$\bar{\sigma}_{pN}^{\text{tot}} = \sigma_{pN}^{\text{tot}} \left(1 - \gamma \frac{7}{5} \frac{E_F}{E} \right), \quad (27)$$

where the Fermi energy E_F is related, in the local density approximation, to the nucleon density $\rho_N(r)$ by $E_F = \frac{\hbar^2}{2m_N} (3\pi^2 \rho_N(r))^{2/3}$. The value of γ is unity according to Ref. [28], but here it is adjusted to reproduce the differential cross section at forward angles. In fact the use of Eq. (27) with $\gamma = 1$ for ^4He turns out to lead to unphysical cross sections because the ^4He density is very large and changes drastically in a small region and thus the local density approximation may not work so well. The adopted value of γ is 0.5 for all He isotopes. At the same time, the range parameter β_{pN} is also appropriately changed as noted in Ref. [14]. The values of V_{so} are kept unchanged. The solid line in Fig. 4 denotes the result of the calculation with the Pauli-blocking correction. Compared to the solid line in Fig. 3 that has no correction, we see that the Pauli-blocking correction results in the decrease of the differential cross sections, leading to fair agreement with experiment at forward angles. The vector analyzing power for ^4He is very much improved as well. Also plotted in Fig. 4 are the results of Ref. [5]

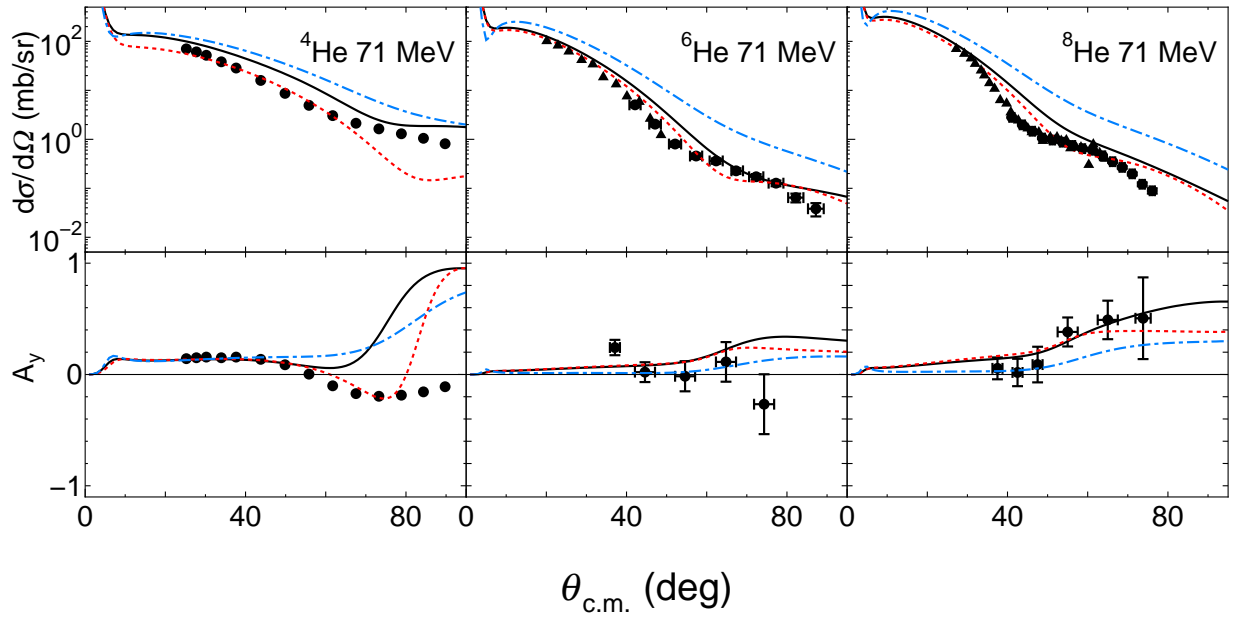


FIG. 3. (Color online) Angular distributions for $p+^{4,6,8}\text{He}$ elastic scattering at 71 MeV. The upper panels show the differential cross sections and the lower panels the vector analyzing powers. Solid lines are full eikonal calculations (10), dotted lines the approximation in the leading-order cumulant expansion (12), and dash-dotted lines the folding model calculations (11). Experimental data are taken from Ref. [7] for ^4He , from Refs. [1, 26] for ^6He , and from Refs. [2, 27] for ^8He .

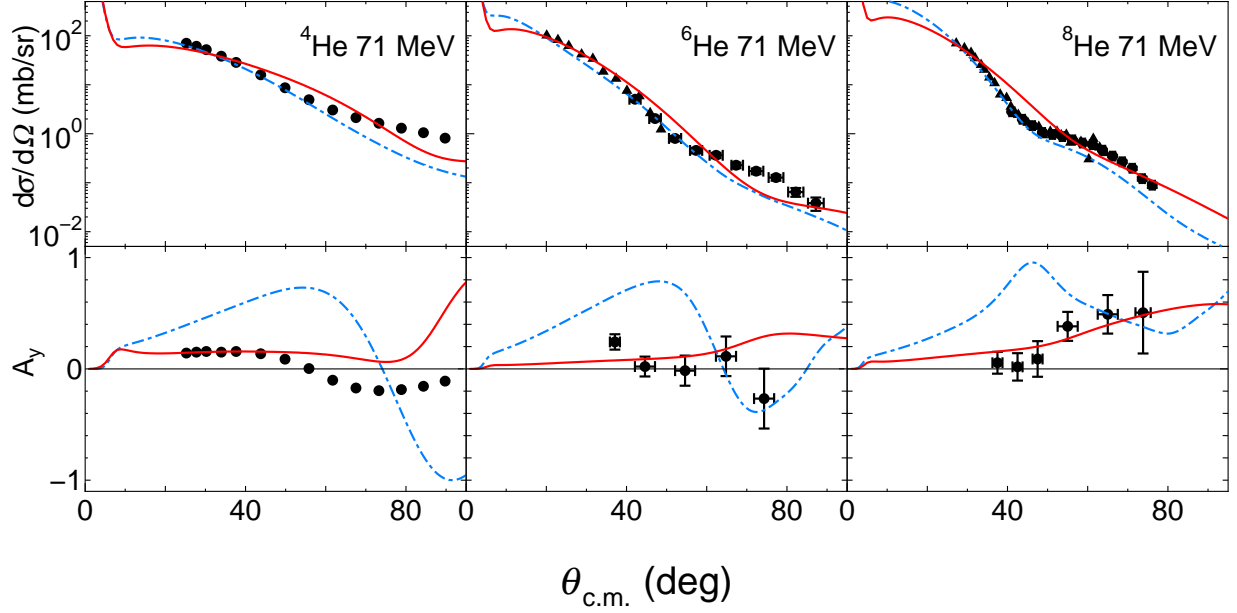


FIG. 4. (Color online) Angular distributions for $p+^{4,6,8}\text{He}$ elastic scattering at 71 MeV compared between calculations and experiment. Solid lines are the results of the present model with the Pauli-blocking effect, while dash-dotted lines are the results taken from Ref. [5]. See the caption of Fig. 3 for the experimental data.

that derives the optical potential based on the Watson formulation of multiple-scattering theory. Our calculation including the breakup effect clearly offers a better description of the scattering of the proton with the He isotopes. The optical potential with the Pauli-blocking

correction is displayed in Fig. 5, and it is compared to the one without the correction. Both real and imaginary parts are reduced significantly for $r < 2$, fm by the Pauli-blocking effect.

As seen in Fig. 4, the theory slightly underestimates

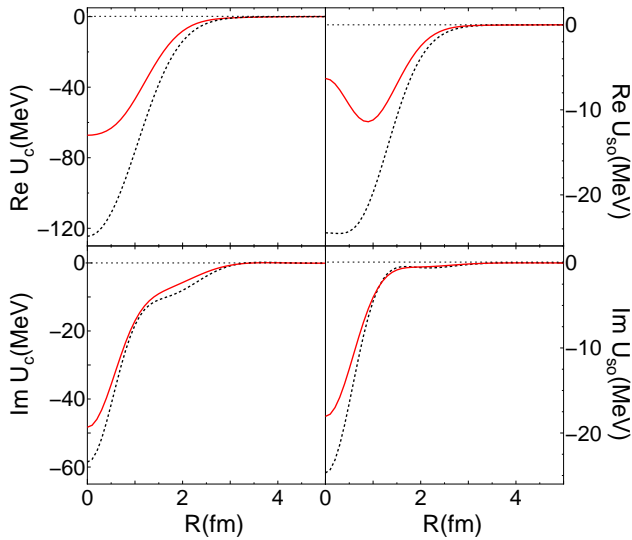


FIG. 5. (Color online) Optical potentials for $p+^4\text{He}$ elastic scattering at 71 MeV. The upper two panels show the central and spin-orbit real potentials while the lower two panels the imaginary potentials. Solid and dotted lines denote the potentials of the full calculation with and without the Pauli-blocking effect, respectively.

the $p+^4\text{He}$ differential cross section beyond 70 degrees. We considered the effect of knock-on process to see whether or not that gives an important contribution in improving the cross section. In the knock-on process the incident nucleon knocks a nucleon inside the nucleus and the knocked nucleon is ejected out of the nucleus. The knock-on exchange effect produces a nonlocal potential and it was calculated assuming a $(0s)^4$ wave function of ^4He and the Minnesota central potential [29]. This nonlocal potential is transformed to an equivalent local potential following the WKB procedure [30]. The effect of this potential is, however, so small that the above discrepancy remains to be resolved.

B. Scattering at 300 and 500 MeV

Next we study the elastic scattering observables at 300 and 500 MeV where $p+^4\text{He}$ data are available for both differential cross sections and vector analyzing powers [31, 32]. The eikonal approximation should work better at these high energies.

Figure 6 displays the optical potentials for proton-elastic scattering from ^4He at 300 and 500 MeV. As already known [11], it is seen that with increasing projectile incident energy the depth of the central real potential decreases and the central imaginary potential increases. The central real potential calculated in the full model at 500 MeV is found to be extremely shallow, which results in a very small real part of the spin-orbit potential if V_{so} is of the order of 0.1. In order to account for the vector analyzing power, V_{so} has to be chosen to be about 1.0 as

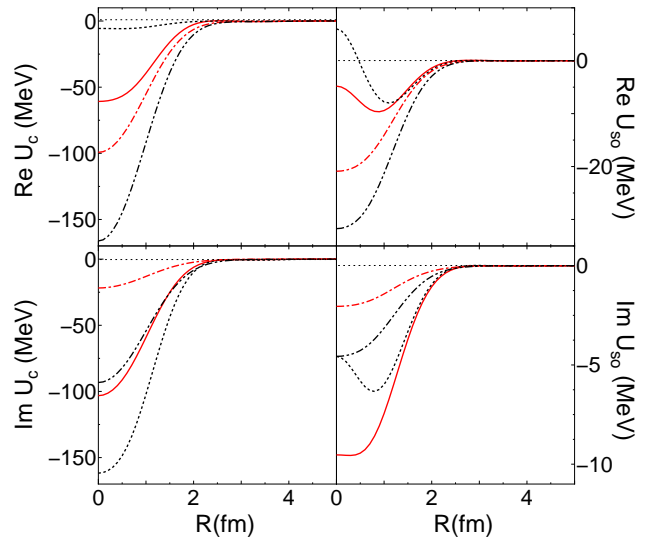


FIG. 6. (Color online) Optical potentials for $p+^4\text{He}$ elastic scattering at 300 and 500 MeV. The upper two panels show the central and spin-orbit real potentials while the lower two panels the imaginary potentials. Solid and dash-dotted lines denote the full and folding potentials at 300 MeV, whereas dotted and dash-dot-dotted lines the full and folding potentials at 500 MeV.

will be shown below.

Figure 7 exhibits observables of proton elastic scattering from ^4He at 300 MeV (left side) and 500 MeV (right side). From the top, differential cross section (a), vector analyzing power (b), and spin-rotation function (c) are given. Dots are experimental data [31] for 300 MeV and [32] for 500 MeV. Note that the theory at 500 MeV is compared to the experiment at 500 MeV. The present theory reproduces both the differential cross section and the vector analyzing power reasonably well.

Finally we predict the scattering observables at 300 MeV for $p+^6\text{He}$ in Fig. 8 and $p+^8\text{He}$ in Fig. 9. Solid and dotted lines in both figures show results for full and folding model calculations. In the case where the real depth parameter V_{so} is chosen to be the same as that of ^4He case at 300 MeV, the angular distributions for ^6He and ^8He are similar to that for ^4He at 300 MeV, as expected. Calculations with two times larger parameter ($V_{\text{so}} = 0.2$) increase the vector analyzing powers at small angles and the differential cross sections at large angles. The differential cross section, the vector analyzing power, and the spin-rotation function are all different between the full and folding model calculations at angles larger than 50 degrees, as we observe in Figs. 3 and 7.

IV. CONCLUSION

We have analyzed the elastic scattering observables for protons scattered from the He isotopes at 71 and 300 MeV. The optical potentials for $p+^{4,6,8}\text{He}$ systems

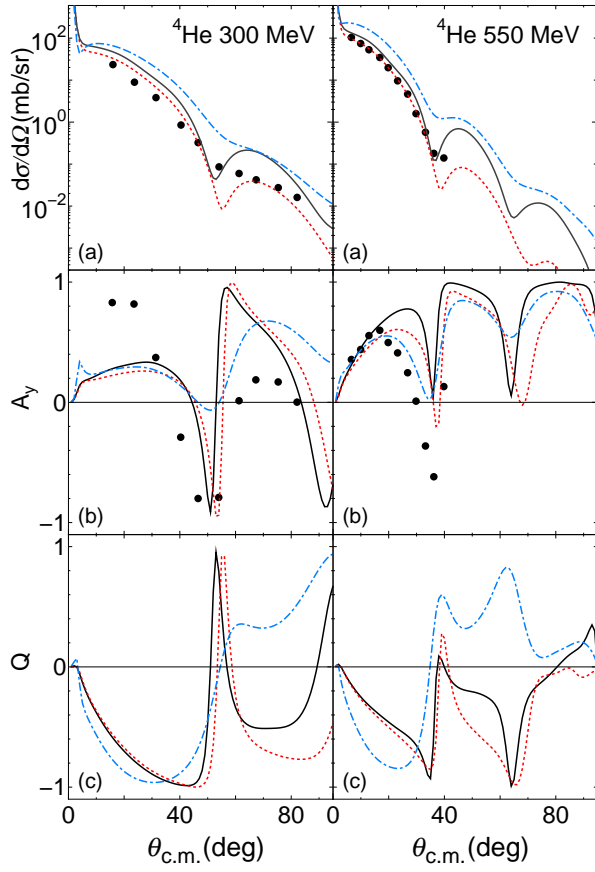


FIG. 7. (Color online) Angular distributions for $p+{}^4\text{He}$ elastic scattering at 300 and 550 MeV. Displayed are the differential cross section (a), the vector analyzing power (b), and the spin-rotation function (c). The values of V_{so} are 0.1 and -0.05 for the real and imaginary potentials at 300 MeV, and 0.9 (0.09 for folding calculation) and -0.025 at 550 MeV. Solid, dotted, and dash-dotted lines indicate the same types of calculations as those of Fig. 3. Experimental data are taken from Ref. [31] for 300 MeV and from Ref. [32] for 550 MeV.

are calculated in the Glauber model. The central potential is evaluated to all orders of the complete Glauber amplitude using the nucleon-nucleon scattering amplitude and the ground-state wave function of the He isotope that is taken from the variational Monte Carlo method. Both the real and imaginary parts of the central potential are determined without any adjustable parameters. It should be noted that the central potential obtained in this way takes into account the breakup effect of the He isotope to its excited states including continuum states, which makes it possible to learn the difference from the single folding model potential. The spin-orbit potential is assumed to take the standard form that uses the derivative of the central potential. Its strength is the only parameter in the present approach.

Though the incident energy of 71 MeV may be a little too low for applying the Glauber theory, the present theory leads us to reasonable agreement with experimen-

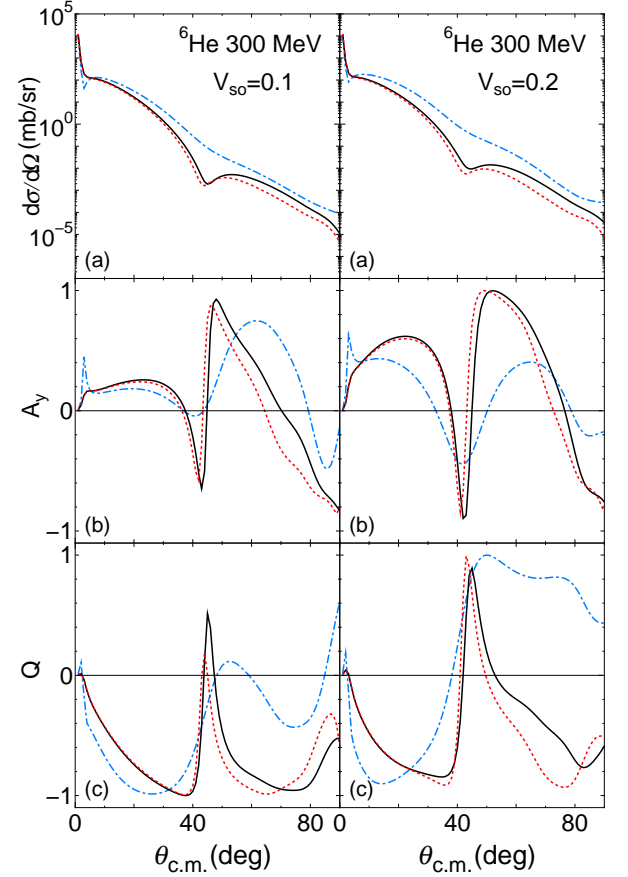


FIG. 8. (Color online) Angular distributions for $p+{}^6\text{He}$ elastic scattering at 300 MeV. The left panels show the results calculated with $V_{\text{so}}=0.1$ for the real potential, the same strength as that of ${}^4\text{He}$ at 300 MeV, while the right panels the results with $V_{\text{so}}=0.2$. The spin-orbit imaginary potential is set to be 0.05, which is the same as that of ${}^4\text{He}$. Solid, dotted, and dash-dotted lines indicate the same types of calculations as those of Fig. 3.

tal data especially on the vector analyzing powers for $p+{}^4,{}^6,{}^8\text{He}$ scatterings simultaneously. It should be noted here that usual t -folding calculations fail to reproduce the vector analyzing powers. We observe that the differential cross sections are all slightly larger than the experimental data even at forward angles. We have studied the Pauli blocking effect that partly suppresses the interaction between the proton and the He isotope and found that including its effect improves the angular distribution of the elastic scattering.

For higher incident energy scattering from ${}^4\text{He}$, the differential cross section is reproduced well at forward angles and the vector analyzing power is also reproduced well in accordance with the experimental data. The vector analyzing power in the intermediate energies has been a long standing problem that defies reproduction of the experimental data. However, the spin-orbit potential given by the derivative of the central potential calculated from the Glauber theory appears to be able to reproduce

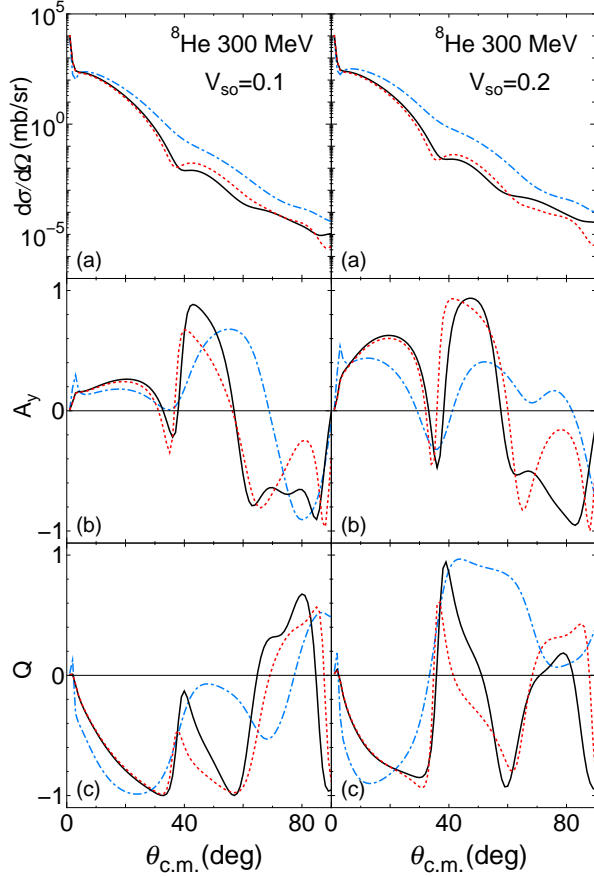


FIG. 9. The same as Fig. 8 but for $p+^8\text{He}$ elastic scattering at 300 MeV.

the proton-elastic scattering in both low and intermediate energy region. We have predicted the angular distributions for $p+^6,^8\text{He}$ elastic scattering at 300 MeV.

V. ACKNOWLEDGMENTS

The authors thank T. Uesaka and S. Sakaguchi for several useful discussions and Ch. Elster for sending them the results of Ref. [5]. The work of Y. S. is supported in part by Grants-in-Aid for Scientific Research (Nos. 21540261 and 24540261) of Japan Society for the Promotion of Science. The work of R. B. W. is supported by the U. S. Department of Energy, Office of Nuclear Physics, under contract DE-AC02-06CH11357.

-
- [1] T. Uesaka *et al.*, Phys. Rev. **C82**, 021602(R) (2010); S. Sakaguchi *et al.*, Phys. Rev. **C84**, 024604 (2011).
 - [2] S. Sakaguchi, Ph. D thesis, Univ. of Tokyo, 2008.
 - [3] R. Crespo, J. A. Tostevin, and R. C. Johnson, Phys. Rev. **C51**, 3283 (1995).
 - [4] L. V. Chulkov, C. A. Bertulani, and A. A. Korsheninikov, Nucl. Phys. **A 587**, 291 (1995).
 - [5] S. P. Weppner, O. Garcia and Ch. Elster, Phys. Rev. **C61**, 044601 (2000); S. P. Weppner and Ch. Elster, Phys. Rev. **C85**, 044617 (2012).
 - [6] N. Keeley and R. S. Mackintosh, Phys. Rev. **C83**, 044608 (2011).
 - [7] S. Burzynski, J. Campbell, M. Hammans, R. Henneck, W. Lorenzon, M. A. Pickar, and I. Sick, Phys. Rev. **C39**, 56 (1989).
 - [8] R. J. Glauber, in *Lectures in Theoretical Physics* (Interscience, New York, 1959), Vol. 1, p. 315.
 - [9] K. Yabana, Y. Ogawa, and Y. Suzuki, Phys. Rev. **C45**, 2909 (1992).
 - [10] Y. Suzuki, R. G. Lovas, K. Yabana, and K. Varga, *Structure and Reactions of Light Exotic Nuclei* (Taylor & Francis, London, 2003).
 - [11] B. Abu-Ibrahim and Y. Suzuki, Nucl. Phys. **A 728**, 118 (2003); Phys. Rev. **C70**, 011603(R) (2004).
 - [12] M. Yahiro, Y. Iseri, H. Kameyama, M. Kamimura, and M. Kawai, Prog. Theor. Phys. Suppl. **89**, 32 (1986); Y. Iseri, M. Yahiro, and M. Kamimura, *ibid.* **89**, 84 (1986).
 - [13] T. Matsumoto, E. Hiyama, K. Ogata, Y. Iseri, M. Kamimura, S. Chiba, and M. Yahiro, Phys. Rev. **C70**, 061601(R) (2004).
 - [14] B. Abu-Ibrahim, W. Horiuchi, A. Kohama, and Y. Suzuki, Phys. Rev. **C77**, 034607 (2008).
 - [15] B. Abu-Ibrahim and Y. Suzuki, Phys. Rev. **C61**, 051601(R) (2000).
 - [16] W. Horiuchi, Y. Suzuki, B. Abu-Ibrahim, and A. Kohama, Phys. Rev. **C75**, 044607 (2007).
 - [17] R. B. Wiringa, V. G. J. Stoks, and R. Schiavilla, Phys. Rev. **C51**, 38 (1995).
 - [18] B. S. Pudliner, V. R. Pandharipande, J. Carlson, and R. B. Wiringa, Phys. Rev. Lett. **74**, 4396 (1995).
 - [19] N. Metropolis, A. W. Rosenbluth, M. N. Rosenbluth, A. H. Teller, and E. Teller, J. Chem. Phys. **21**, 1087 (1953).
 - [20] R. B. Wiringa, S. C. Pieper, J. Carlson, and V. R. Pandharipande, Phys. Rev. **C62**, 014001 (2000).
 - [21] R. B. Wiringa, Phys. Rev. **C43**, 1585 (1991).
 - [22] B. S. Pudliner, V. R. Pandharipande, J. Carlson, S. C. Pieper, and R. B. Wiringa, Phys. Rev. **C56**, 1720 (1997).

- [23] P. Mueller *et al.*, Phys. Rev. Lett. **99**, 252501 (2007); M. Brodeur *et al.*, Phys. Rev. Lett. **108**, 052504 (2012).
- [24] K. Varga, S. C. Pieper, Y. Suzuki, and R. B. Wiringa, Phys. Rev. C **66**, 034611 (2002).
- [25] A. Bohr and B. R. Mottelson, *Nuclear Structure* (Benjamin, New York, 1969), Vol. I
- [26] A. A. Korshennikov *et al.*, Nucl. Phys. **A 617**, 45 (1997).
- [27] A. A. Korshennikov *et al.* Phys. Lett. **B316**, 38 (1993).
- [28] M. S. Hussein, R. A. Rego, and C. A. Bertulani, Phys. Rep. **201**, 279 (1991).
- [29] D. R. Thompson, M. LeMere, and Y. C. Tang, Nucl. Phys. **A 286**, 53 (1977);
- [30] H. Horiuchi, Prog. Theor. Phys. **64**, 184 (1980).
- [31] M. Yoshimura *et al.*, Phys. Rev. C **63**, 034618 (2001).
- [32] S. M. Sterbenz *et al.*, Phys. Rev. C **45**, 2578 (1992).